Pattern formation and self-assembly driven by competing interactions

Davide Pini[1] and Alberto Parola[2]

[1]*Dipartimento di Fisica, Università di Milano,*
Via Celoria 16, 20133 Milano, Italy

[2]*Dipartimento di Scienza e Alta Tecnologia,*
Università dell'Insubria, Via Valleggio 11, 22100, Como, Italy

Abstract

Colloidal fluids interacting via effective potentials which are attractive at short range and repulsive at long range have long been raising considerable attention, because such an instance provides a simple mechanism leading to pattern formation even for isotropic interactions. If the competition between attraction and repulsion is strong enough, the gas-liquid phase transition is suppressed, and replaced by the formation of mesophases, i.e., inhomogeneous phases displaying periodic density modulations whose length, although being larger than the particle size, cannot nevertheless be considered macroscopic. We describe a fully numerical implementation of density-functional theory in three dimensions, tailored to periodic phases. The results for the equilibrium phase diagram of the model are compared with those already obtained in previous investigations for the present system as well as for other systems which form mesophases. The phase diagram which we find shows a strong similarity with that of block copolymer melts, in which self-assembly also results from frustration of a macroscopic phase separation. As the inhomogeneous region is swept by increasing the density from the low-density side, one encounters clusters, bars, lamellae, inverted bars, and inverted clusters. Moreover, a bicontinuous gyroid phase consisting of two intertwined percolating networks is predicted in a narrow domain between the bar and lamellar phases.

I. INTRODUCTION

Soft matter often displays remarkably complex phase behaviors stemming from the competition between different strategies to minimize the free energy. The simultaneous presence of hydrofobic and hydrophilic interactions in amphiphilic molecules, like surfactants, leads to micellization [1], while repulsion between unlike sequences in block copolymers drives the formation of nanostructures [2]. Even the presence of purely repulsive and isotropic interactions may lead to complex patterns: branched molecules, like dendrimers, form cluster crystals [3, 4], while hard-core particles surrounded by a soft corona, also known as "soft shoulder systems", display a remarkably rich set of ordered phases [5]. Understanding the relation between effective interactions among units (colloidal particles, globular polymers, branched molecules, proteins, etc.) and the mesoscopic structures formed in solution is an important and challenging problem of soft matter with foreseeable technological implications in diverse fields, allowing for the design of specific porous materials on the nanoscale.

Charged colloidal particles are ubiquitous in soft matter physics. When electrostatic repulsion is combined to the short-range attraction which characterizes most of the colloidal suspensions or protein solutions, it gives rise to a flexible mechanism for designing complex structures from the nano to the micro scale. Competing interactions, by inhibiting phase separation, make ample portions of phase space available for different and more elaborate forms of self assembly. For this reason, in recent years short-range attractive, long-range repulsive (SALR) systems have been the subject of intense research starting from the seminal work by Sear *et al.* [6] where the spontaneous formation of two-dimensional spatially modulated phases of nanoparticles deposited at the air-water interface was investigated both experimentally and theoretically. Numerical simulations on a simple two-dimensional model of SALR fluid were performed [7], confirming the tendency to cluster formation in the homogeneous phase and the presence of ordered phases displaying one- or two-dimensional modulations in the particle density, giving rise to a characteristic stripe pattern in the first case and a triangular cluster arrangement in the second.

Density-functional theory (DFT), based on a simple mean-field approximation, allowed to determine the phase diagram of this model, highlighting the presence of several local minima in the free energy corresponding to structures characterized by the presence of defects [8]. These findings suggest the possible occurrence of metastable phases in the reported experiments, although a proper investigation of these non-equilibrium long-lived states requires the use of alternative theoretical tools. Self-assembly of SALR systems in three dimensions is a more challenging problem, both on the theoretical and on the experimental side. Evidence of cluster formation has been collected in colloid-polymer mixtures [9] but the formation of equilibrium periodic structures is often inhibited by dynamical arrest. Accurate chemical stabilization of the colloidal particles is required to perform controlled experiments. Numerical simulations suffer from similar problems: metastability of cluster phases is a challenge also at the numerical level and few numerical experiments have been performed to date [10]. Only recently some evidence of periodic phases in three-dimensional SALR fluids has been obtained by simulation [11].

A perturbative analysis of DFT for small deviations of the local density from the homogeneous state has been carried out by several authors, following the analog treatment for block copolymers [2]. In particular, Ciach and co-workers developed a general formalism able to predict the sequence of ordered phases expected in systems characterized by competing interactions [12], while the occurrence of correlated clusters in the fluid phase has been recently investigated by numerical simulations and thermodynamic models [13]. Density-functional theory (DFT) [14] can be directly applied to microscopic models of fluids leading to a quantitative prediction of the phase diagram and the stable equilibrium structures. However, the numerical minimization of the density functional is computationally demanding in three-dimensional models, and the numerical algorithm is often trapped in local minima [15]. Such a difficulty is probably related to the lack of commensurability between the (unknown) equilibrium structure and the finite volume where the fluid is confined.

We recently tackled this problem by developing an adaptive algorithm, where periodic conditions are imposed at the boundary of the confining volume, whose shape

and size are self-consistently determined by the algorithm itself extending the basic idea put forward by Parrinello and Rahman in molecular dynamics [16]. Our method was first applied [17] to a system of particles interacting via a soft-core, repulsive potential introduced in Ref. [4] as a model of amphiphilic dendrimers in solution and subsequently [18] to a binary fluid of particles with repulsive Gaussian potentials, which can be viewed as a modellization of a mixture of globular polymers and had been proved to be capable of forming cluster phases for suitably chosen interaction parameters [19]. While in the former case the resulting picture was basically the same as that obtained in previous investigations of similar systems leading to cluster crystals [3], the study of the Gaussian mixture brought forth an unexpectedly rich phase diagram featuring bicontinuous phases and other exotic structures, which would have been quite difficult to recover, had the density profile been chosen *a priori* within a given pool of candidates.

In this paper, we have employed the same DFT algorithm to study a SALR model fluid in three dimensions. A DFT investigation of this system based on an algorithm similar to that used here has recently been performed [20]. The results so far available show the same sequence of phases predicted by the perturbative analysis carried out by Ciach *et al.* [12], which in turn is the same as that previously obtained in block copolymers [2]. Indeed, it has been pointed out that such a sequence is to be expected in a wide class of mesophase-forming fluids [21] and, not surprisingly, we obtain it here as well. Accordingly, while the description of the phase diagram is part of the present study, we tried not to place its main emphasis on this topic, as it would not convey much new information with respect to what already brought forth in former investigations. Instead, we addressed also a number of questions which have been given less attention, such as: how do the density profiles compare with those obtained by the perturbative approach? For a given phase, how do the mutual distance between the aggregates, their size, and the particle density inside each aggregate change as the temperature and average density are varied? How are these features affected by moving from a phase to another? Answering these questions can help to get a more complete picture of mesophase formation in SALR fluids, and to understand

the mechanism which causes the sequence of mesophases commonly observed in these as well as other systems.

It is worthwile mentioning that an analytical study of the DFT mean-field equations allows to draw a general picture of mesophase formation in a wide class of one component fluids: starting from a limited number of simplifying assumptions, the correct sequence of ordered phases is recovered both for hard-core and soft-core systems and some universal feature of the resulting density modulations are obtained [22].

The paper is organized as follows: in Sec. II we introduce the model potential and briefly describe the density functional and the minimization algorithm which we have adpoted. Our results for the phase diagram, the density profiles, and the influence of the thermodynamic state on phase morphology are presented in Sec. III. Finally, in Sec. IV we summarize the main points of this study and draw our conclusions.

II. THEORY

We consider a fluid of particles interacting via a two-body, spherically symmetric potential $u(r)$ which consists of a hard core followed by a short-range attractive and longer-ranged repulsive tail $w(r)$. This SALR tail has been modeled as the sum of two Yukawa functions with opposite signs. We have then

$$u(r) = \begin{cases} \infty & r < \sigma \\ \dfrac{\sigma}{r}\left[-\epsilon e^{-z_1(r/\sigma-1)} + Ae^{-z_2(r/\sigma-1)}\right] & r \geq \sigma\,, \end{cases} \tag{1}$$

where σ is the hard-core diameter, ϵ is the attraction strength, A is the repulsion strength, and z_1, z_2 are the inverse-range parameters of the attraction and repulsion respectively. From now on, lengths will be measured in units of σ, energies in units of ϵ, and the reduced quantities thus obtained will be denoted by an asterisk.

In order to describe a SALR interaction, one must obviously have $A > 0$, $z_1 > z_2$. Here we have set $z_1 = 1$, $z_2 = 0.5$. As for A, we have followed Ref. [7] by choosing

A in such a way that the integrated intensity of the SALR tail vanishes. In doing so, we have adopted the standard prescription of fixing the tail inside the hard-core region at its minimum $-\epsilon + A$. We then obtain $A^* = 7/19 \simeq 0.368$. This value of A corresponds to a vanishing liquid-vapor critical temperature according to the van der Waals approximation, to which the mean-field functional used here reduces in the homogeneous case. Hence, we are safely in the regime in which the liquid-vapor transition is preempted by the competition between attraction and repulsion. We remark that in the present study, the interaction profile has been kept fixed, and its strength has been changed by varying the temperature T. This is different from the procedure followed in other studies of SALR interactions [10, 23, 24], in which ϵ was changed, whereas A and T were kept fixed. In the latter case, as the attraction increases, we expect that the liquid-vapor transition will eventually take over.

A plot of $u(r)$ has been displayed in Fig. 1. Clearly, for the present choice of parameters the repulsive hump is very low, to the point that it is barely visible on the scale of the figure. However, the effect of competition becomes evident by turning to Fourier space. As shown in the inset, the Fourier transform of the off-core part of the potential $\widetilde{w}(k)$ has its absolute minimum at a non vanishing wave vector $k_0^* \simeq 0.655$, hence favoring spontaneous density modulations. In the homogeneous phase, this feature is signaled by the occurrence of a peak at $k \simeq k_0$ in the structure factor $S(k)$ due to the tendency of particles to aggregate into equilibrium clusters with an average inter-cluster distance $d \sim 2\pi/k$. As the temperature is lowered, the homogeneous phase eventually becomes unstable, and the system forms regular structures whose periodicity is again of the order of d, typically much larger than the particle size σ.

The present investigation concerns the study of these inhomogeneous phases by DFT. At a given temperature T, chemical potential μ, and volume V, the density profile is obtained by minimizing the grand potential functional $\Omega[\rho(\mathbf{r})]$, whose value then yields the grand potential $-PV$, where P is the pressure. Henceforth, the density profile will be denoted by $\rho(\mathbf{r})$, while ρ with no point-dependence indicated will refer to the average density $\rho \equiv \int d^3\mathbf{r}\rho(\mathbf{r})/V$. Here we have adopted a simple
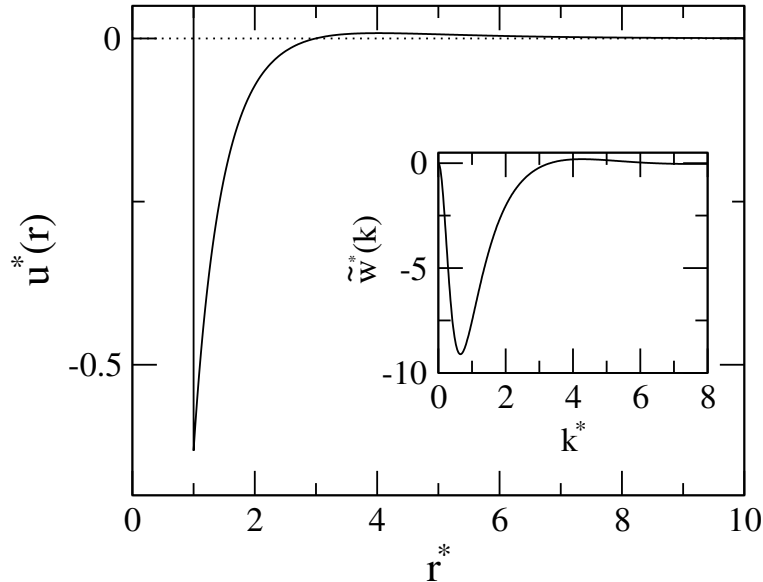
FIG. 1: SALR potential $u(r)$ of Eq. (1) for the interaction parameters specified in the text. The inset displays the Fourier transform of the SALR tail $\widetilde{w}(k)$, showing its absolute minimum at $k \neq 0$. All quantities are in reduced units.

functional, in which the contributions to the grand potential due to the hard-sphere interaction and the SALR tail $w(r)$ are treated respectively in the local-density and mean-field approximations, and $\Omega[\rho(\mathbf{r})]$ is given by

$$\Omega = \int d^3\mathbf{r} \, \{f_{\mathrm{HS}}[\rho(\mathbf{r})] - \mu \, \rho(\mathbf{r})\} + \frac{1}{2} \int d^3\mathbf{r} \int d^3\mathbf{r}' \rho(\mathbf{r})\rho(\mathbf{r}')w(\mathbf{r} - \mathbf{r}') \,, \qquad (2)$$

where f_{HS} is the Helmholtz free energy per unit volume of the hard-sphere fluid. The latter has been described by the standard Carnahan-Starling expression [14] throughout this study.

The above functional is the straightforward generalization to an inhomogeneous fluid of the van der Waals approximation for Ω, which as pointed out above is recovered in the homogeneous case $\rho(\mathbf{r}) \equiv \rho$. Functional (2) has already been employed to study mesophase formation in two-dimensional SALR fluids [8]. An application to the three-dimensional case was also considered [24] which, however, was limited to lamellar phases where $\rho(\mathbf{r})$ varies along a single direction. As discussed there, for

7

mesophases such that the characteristic length of the density modulations is much larger than σ, the local-density approximation (LDA) for the hard-sphere free-energy functional is expected to be sufficiently accurate. A better description of the hard-sphere term would instead be necessary in order to describe the structure inside the mesoscopic aggregates, where particles are expected to form packed arrangements resulting in short-length modulations of order $\sim \sigma$, as well as the occurrence of a crystal phase driven by excluded-volume effects, expected at high density. Such a development was in fact considered in Ref. [20], where the contribution to the free energy due to the SALR tail was taken into account by the same mean-field expression of Eq. (2), but the hard-sphere part was described by fundamental measure theory (FMT) [25]. We also recall that a mean-field functional similar to Eq. (2) has proved quite successful in the study of cluster crystals occurring in systems with purely soft-core repulsive interactions [26, 27]. In that case, of course, f_{HS} is replaced by the Helmholtz free energy per unit volume of the ideal gas, for which the LDA is exact.

For a homogeneous state, the stability condition with respect to a small perturbation of the density $\delta\rho(\mathbf{r})$

$$\int d^3\mathbf{r} \int d^3\mathbf{r}' \left. \frac{\delta^2 \Omega}{\delta\rho(\mathbf{r})\delta\rho(\mathbf{r}')} \right|_\rho \delta\rho(\mathbf{r})\delta\rho(\mathbf{r}') > 0 \tag{3}$$

is equivalent to the requirement $\widetilde{c}(k) < 0$ for every wave vector k, where $\widetilde{c}(k)$ is the Fourier transform of the direct correlation function $c(r)$ of the homogeneous fluid, inclusive of the ideal-gas term. Functional differentiation of Eq. (2) gives

$$\widetilde{c}(k) = -\frac{1}{\rho \chi_{\mathrm{red}}^{\mathrm{HS}}(\rho)} - \frac{\widetilde{w}(k)}{k_{\mathrm{B}}T} , \tag{4}$$

where k_{B} is the Boltzmann constant, and $\chi_{\mathrm{red}}^{\mathrm{HS}}$ is the reduced isothermal compressibility of the hard-sphere fluid. We remark that Eq. (4) can be considered as a rougher version of the standard random-phase approximation (RPA) for $\widetilde{c}(k)$, such that the dependence on k of the hard-sphere contribution $\widetilde{c}_{\mathrm{HS}}(k)$ is disregarded by setting it identically to its value at $k = 0$. In order to recover the genuine RPA, a non-local functional for the hard-sphere fluid such as the aforementioned FMT is necessary.

According to Eq. (4), at low temperature the condition $\widetilde{c}(k) < 0$ is violated inside a certain density interval. The boundary of the domain in the ρ–T plane where the homogeneous phase becomes unstable is defined, for any fixed density, by the highest temperature at which $\widetilde{c}(k)$ vanishes and is given by the curve

$$\frac{k_{\mathrm{B}}T}{w_0} = \rho \chi_{\mathrm{red}}^{\mathrm{HS}}(\rho) \,, \tag{5}$$

where $w_0 \equiv |\widetilde{w}(k_0)|$ is the absolute value of the minimum of $\widetilde{w}(k)$. For the interaction parameters specified above, one has $w_0^* \simeq 9.108$. Along this curve, often referred to as the λ-line, the structure factor $S(k) = -1/[\rho \widetilde{c}(k)]$ diverges at k_0. The λ-line is then akin to the spinodal curve of the liquid-vapor transition. In fact, within the present approximation the two curves have the same expression, save for the fact that the spinodal is obtained for $k_0 = 0$, of course assuming that $\widetilde{w}(0)$ is strictly negative. For the case in hand, the spinodal is absent since $\widetilde{w}(0)$ vanishes.

In order to obtain further insight in the phase diagram and the structure of the inhomogeneous phases, it is necessary to turn to the minimization of functional (2). Here we have assumed from the outset that the density profile $\rho(\mathbf{r})$ is periodic, i.e.

$$\rho(\mathbf{r} + \mathbf{a}_i) = \rho(\mathbf{r}) \,, \tag{6}$$

where $\mathbf{a}_i$, $i = 1$, 2, 3, are a set of vectors which define a Bravais lattice. Therefore, $\rho(\mathbf{r})$ can be expanded in a Fourier series:

$$\rho(\mathbf{r}) = \frac{1}{v} \sum_{\mathbf{m}} e^{-i\mathbf{k_m} \cdot \mathbf{x}} \, \hat{\rho}_{\mathbf{m}} \,, \tag{7}$$

where v is the volume of the unit cell, $\mathbf{k_m}$ is a vector of the reciprocal lattice, and $\mathbf{m}$ denotes a set of three integers m_i, $i = 1, 2, 3$, $m_i = 0, \pm 1, \pm 2 \ldots$. The expansion coefficients $\hat{\rho}_{\mathbf{m}}$ are given by:

$$\hat{\rho}_{\mathbf{m}} = \int_v d^3 \mathbf{r} \, e^{i\mathbf{k_m} \cdot \mathbf{r}} \rho(\mathbf{r}) \,. \tag{8}$$

By use of Eqs. (6) and (7), functional (2) can be rewritten in the following form:

$$\frac{\Omega}{V} = \frac{1}{v} \int_v d^3 \mathbf{r} \, \{f_{\mathrm{HS}}[\rho(\mathbf{r})] - \mu \, \rho(\mathbf{r})\} + \frac{1}{2v^2} \sum_{\mathbf{m}} |\hat{\rho}_{\mathbf{m}}|^2 \, \widetilde{w}(\mathbf{k_m}) \,. \tag{9}$$

9

We observe that, in both Eqs. (8) and (9), the integration in $\mathbf{r}$ is restricted to the unit cell. Hence, we may set $\mathbf{r} = \mathbf{A} \cdot \mathbf{s}$, where $\mathbf{A} \equiv (\mathbf{a}_1, \mathbf{a}_2, \mathbf{a}_3)$ is the matrix obtained by arranging the lattice vectors $\mathbf{a}_i$ into columns, and $\mathbf{s}$ is a vector whose components vary in the interval $[-1/2, 1/2)$. By doing so, it is readily seen that in Eq. (9) neither the hard-sphere term nor the Fourier components of the density profile $\hat{\rho}_{\mathbf{m}}$ that appear in the excess term depend on the specific kind of lattice: that is, these quantities are determined solely by the values $\rho(\mathbf{s}) \equiv \rho(\mathbf{A} \cdot \mathbf{s})$ assumed by the density profile in the unit cell, irrespective of the cell geometry. The information on the lattice enters in Eq. (9) *only* via the reciprocal lattice vectors $\mathbf{k}_{\mathbf{m}}$ at which $\widetilde{w}(k)$ is evaluated. This feature makes it easy to implement a numerical procedure, in which the optimization of the grand potential functional (9) is performed with respect to both $\rho(\mathbf{s})$ and the cell geometry, i.e., the elements of $\mathbf{A}$. In this study, we have assumed that the vectors $\mathbf{a}_i$ of the unit cell are mutually orthogonal, so that $\mathbf{A}$ is diagonal with eigenvalues $2\pi/h_i$, and the reciprocal lattice vectors $\mathbf{k}_{\mathbf{m}}$ have the form $\mathbf{k}_{\mathbf{m}} = (h_1 m_1, h_2 m_2, h_3 m_3)$. This assumption simplifies the calculation, but it could be released without introducing any conceptually new element.

To perform the minimization, one has to solve the Euler-Lagrange equations $\delta(\Omega/V)/\delta\rho(\mathbf{r}) = 0$ as well as $\partial(\Omega/V)/\partial h_i = 0$, where the functional derivative with respect to $\rho(\mathbf{r})$ and the partial derivative with respect to h_i are given by:

$$\frac{\delta}{\delta\rho(\mathbf{r})}\left(\frac{\Omega}{V}\right) = \frac{1}{v}\left\{f'_{\mathrm{HS}}[\rho(\mathbf{r})] - \mu\right\} + \frac{1}{v^2}\sum_{\mathbf{m}} e^{-i\mathbf{k}_{\mathbf{m}}\cdot\mathbf{r}}\hat{\rho}_{\mathbf{m}}\,\widetilde{w}(\mathbf{k}_{\mathbf{m}})\,, \tag{10}$$

$$\frac{\partial}{\partial h_i}\left(\frac{\Omega}{V}\right) = \frac{1}{v^2}\sum_{\mathbf{m}}|\hat{\rho}_{\mathbf{m}}|^2\frac{d\widetilde{w}}{d(k^2)}(\mathbf{k}_{\mathbf{m}})\,h_i m_i^2\,, \tag{11}$$

where f'_{HS} denotes the first derivative of f_{HS} with respect to ρ.

In the numerical solution, $\Omega[\rho(\mathbf{r})]$ was first discretized by sampling $\rho(\mathbf{r})$ on a finite set of points $\rho_{\mathbf{n}}$, so as the replace the functional derivatives with the partial derivatives with respect to $\rho_{\mathbf{n}}$. The minimization was then carried out by an iterative algorithm based on the steepest descent. In the basic version of the steepest descent, $\rho_{\mathbf{n}}$ and h_i are updated recursively by moving "downhill" in the direction opposite to that of

the gradient of the discretized functional Ω_D:

$$\rho_{\mathbf{n}}^{k+1} = \rho_{\mathbf{n}}^k - \eta \frac{\partial}{\partial \rho_{\mathbf{n}}} \left(\frac{\Omega_D}{V} \right) \bigg|_k , \tag{12}$$

$$h_i^{k+1} = h_i^k - \theta \frac{\partial}{\partial h_i} \left(\frac{\Omega_D}{V} \right) \bigg|_k , \tag{13}$$

where k is the iteration index, and η, θ are the parameters which determine the size of the downhill step. In order to increase its efficiency, the above algorithm was improved by introducing preconditioning and conjugate gradients in Eq. (12), and by determining the step-size parameters η, θ adaptively at each iteration. A detailed description of these technical features has been given elsewhere [18].

The discretization of the density profile $\rho(\mathbf{r})$ inside the unit cell was performed on $2^7 \times 2^7 \times 2^7 = 2\,097\,152$ points. The cell in real space was initially chosen as a cube with edge length $2\pi/h_i = 20\sigma$, and was then evolved according to Eq. (13). The trial density profile $\rho_{\text{trial}}(\mathbf{r})$ used to start the minimization at a given thermodynamic state was set either to a random noise superimposed to a uniform density, or to a sinusoidal modulation, or to the equilibrium $\rho(\mathbf{r})$ of a nearby state. In general, for a certain chemical potential μ, different inhomogeneous structures were found, especially in the neighborhood of the boundaries between different phases. The most stable phase was identified as that giving the lowest value of $\Omega/V = -P$ at given μ, and phase coexistence between two phases 1 and 2 was determined by the conditions $\mu_1 = \mu_2$, $P_1 = P_2$ at given T.

III. RESULTS

A. The topology of the ordered phases

The phase diagram in the temperature-density plane obtained by implementing the minimization algorithm described in Sec. II is shown in Fig. 2. As already found in previous investigations of the SALR fluid in two [8] and three [12] dimensions, the inhomogeneous region is larger than the domain of instability of the homogeneous
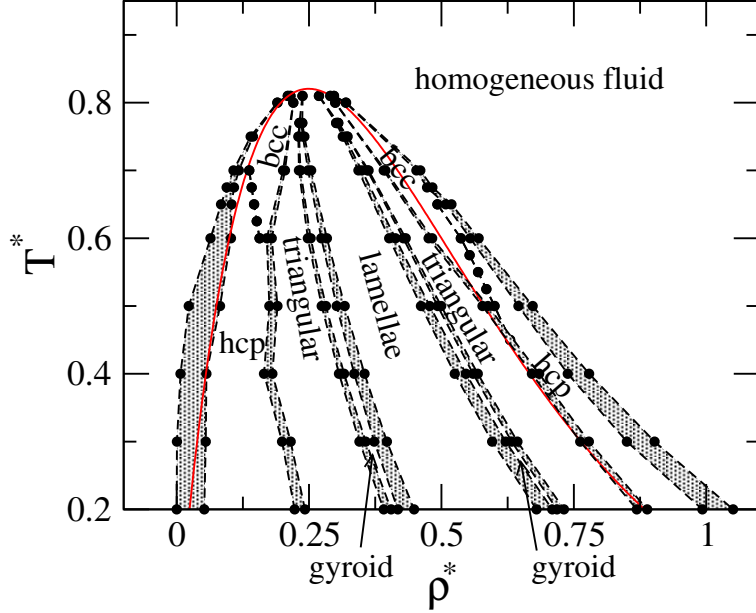
FIG. 2: Phase diagram of the SALR HCTYF fluid with interaction parameters specified in Sec. II in the temperature-density plane. Both quantities are in reduced units. The filled circles represent the phase boundaries obtained by numerical minimization of functional (2). The dashed lines are a guide for the eye. The grey shaded regions are coexistence domains. The red solid line is the λ-line.

fluid bounded by the λ-line, and the two merge only at the top. All the boundaries between the phases displayed in the Figure correspond to first-order transitions, except for that between the homogeneous fluid and the lamellar phase at the top of the λ-line, for which the mean-field functional used here necessarily predicts a second-order transition [2]. The coexistence regions between different phases have been indicated in grey.

The sequence of phases agrees qualitatively with that formerly established by effective free-energy functionals [12, 21, 28], numerical simulation [11], and numerical DFT minimization along the same lines pursued here [20]. Figures 3–9 show the sequence of phases along the isotherm $T^* = 0.6$. Each phase has been portrayed inside a unit cell by displaying in yellow the isosurfaces at which $\rho(\mathbf{r})$ attains some constant value ρ_{iso} specified in the captions. The regions such that $\rho(\mathbf{r}) > \rho_{\text{iso}}$ have

been represented by their intersections with the cell faces, with a color map ranging from red (higher density) to green (lower density). The figures have been produced by the VESTA software [29].

The central region of the phase diagram is inhabited by a lamellar phase whose density profile varies only along a single direction, see Fig. 3. The rest of the phase diagram displays a symmetry of sorts with respect to this domain. As one moves from the homogeneous fluid at low density to the inhomogeneous fluid, one finds first a triply-periodic cluster phase such as that of Fig. 4. At sufficiently high temperature, the clusters are arranged into a bcc lattice, whereas as the temperature is lowered, a hcp lattice is preferred. According to a rough estimate obtained by dividing the number of particles in a unit cell by the number of peaks of the density profile, each cluster typically contains several hundreds of particles. The cluster phase is
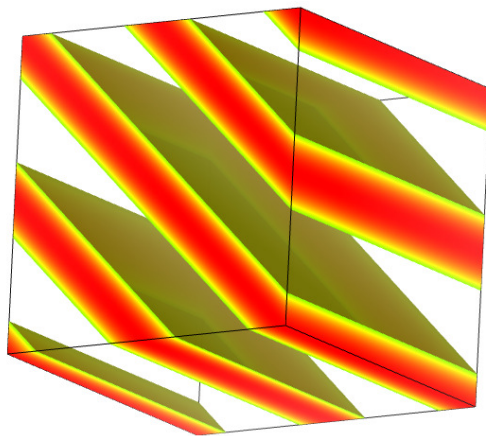
FIG. 3: A section of the density profile of the lamellar phase at $T^* = 0.6$, $\rho^* = 0.37$, $\rho^*_{\mathrm{iso}} = 0.45$.

mirrored by the inverted-cluster phase of Fig. 5 encountered when one enters the inhomogeneous region from high density. In this phase clusters are replaced by holes depleted of particles, which then accumulate in the space between the holes in a "Swiss-cheese" arrangement. Like the clusters of the "direct" phase, holes too form either a bcc or a hcp lattice at respectively high and low temperature.

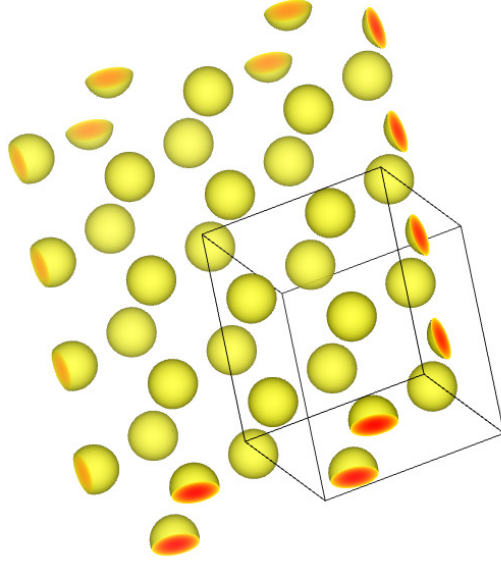As one moves from the cluster phase to higher density, the system experiences

FIG. 4: A section of the density profile of the bcc cluster phase at $T^* = 0.6$, $\rho^* = 0.13$, $\rho^*_{\mathrm{iso}} = 0.58$.

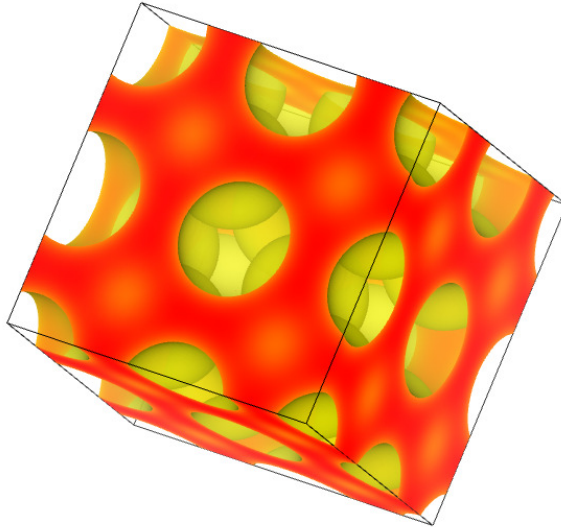

FIG. 5: A section of the density profile of the bcc inverted-cluster phase at $T^* = 0.6$, $\rho^* = 0.52$, $\rho^*_{\mathrm{iso}} = 0.58$.

a transition to a doubly-periodic configuration such that the density profile has cylindrical symmetry. Clusters are then replaced by cylindrical bars, which form a two-dimensional equilateral triangular lattice as shown in Fig. 6. Conversely, the

inverted-cluster phase is replaced at lower density by a triangular inverted-cylinder phase with particle-depleted domains in the shape of cylindrical holes, and particles percolating in the region between them, see Fig. 7.
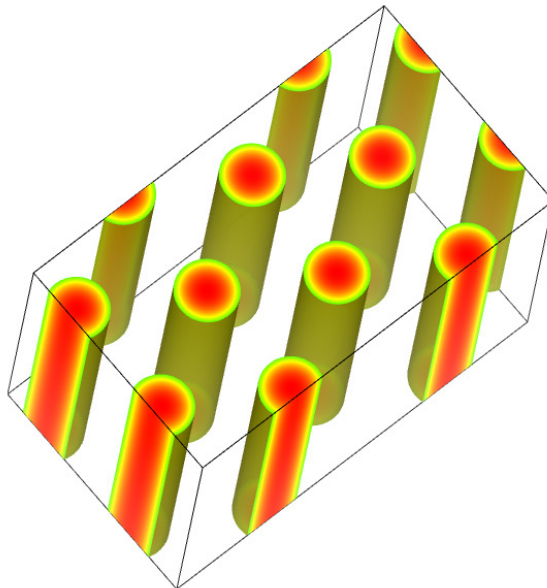

FIG. 6: A section of the density profile of the triangular bar phase at $T^* = 0.6$, $\rho^* = 0.22$, $\rho^*_{\text{iso}} = 0.44$.
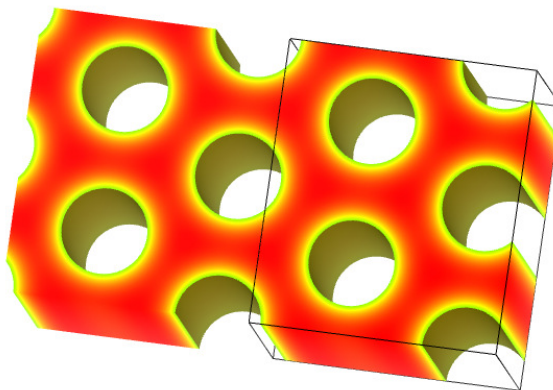

FIG. 7: A section of the density profile of the triangular inverted-bar phase at $T^* = 0.6$, $\rho^* = 0.47$, $\rho^*_{\text{iso}} = 0.44$.

Finally, by moving further towards the lamellar region, either from low or high densities, one finds two narrow domains where particles arrange into a double-gyroid

bicontinuous configuration. Unlike in the case of direct and inverted clusters or cylinders, the similarity between filled and depleted domains of phases symmetric with respect to the lamellar region is not clearly apparent from Figs. 8 and 9. However, this feature is still there, although in order to bring it forward, one has to specify rather different values of ρ_{iso} in the two phases. Specifically, Figs. 8 and 9 refer to $\rho^* = 0.26$ and $\rho^* = 0.42$ respectively, and correspond to the same $\rho_{\mathrm{iso}}^* = 0.65$. The inverted configuration with respect to that of Fig. 8 for the state at $\rho^* = 0.42$ is obtained for $\rho_{\mathrm{iso}}^* \simeq 0.05$. Similarly, by setting again $\rho_{\mathrm{iso}}^* \simeq 0.05$ for the state at $\rho^* = 0.26$, one obtains the inverted configuration with respect to that of Fig. 9.
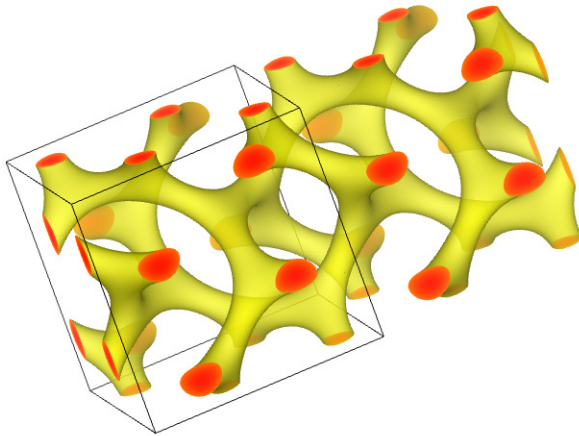

FIG. 8: A section of density profile of the double-gyroid phase at $T^* = 0.6$, $\rho^* = 0.26$, $\rho_{\mathrm{iso}}^* = 0.65$.

As pointed out above, the overall phase portrait has been by now firmly established in former investigations [11, 12, 20, 21, 28]. Nevertheless, two features of the phase diagram of Fig. 2 may be worth pointing out: first, the gyroid domain obtained here is much narrower than that predicted for similar SALR systems by effective free-energy functionals [12, 20], especially on the high-density side of the lamellar region. Second, the presence of both a bcc and a hcp lattice for the cluster and inverted-cluster phases was not reported in those studies, where only the bcc lattice was obtained. Not surprisingly, we found that the hcp phase is in close competition with a fcc phase of nearly the same free energy. In fact, such a fcc phase has been observed in numerical simulations of a SALR potential consisting in an attractive square well
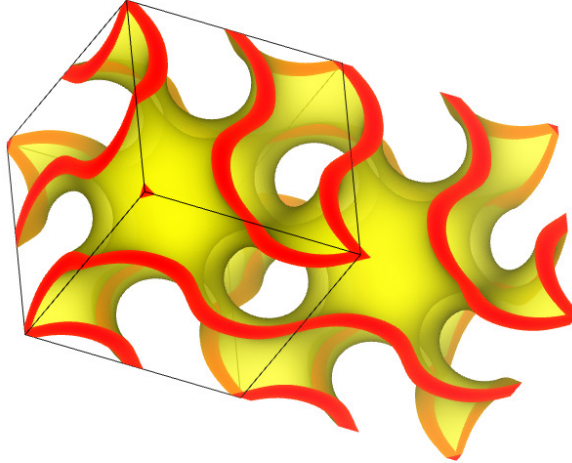
FIG. 9: A section of the density profile of the double-gyroid phase at $T^* = 0.6$, $\rho^* = 0.42$, $\rho^*_{\mathrm{iso}} = 0.65$.

followed by a repulsive ramp [11]. The existence of both bcc and hcp cluster phases was also predicted in block copolymers by self-consistent field theory calculations [30]. In the weak-segregation regime, corresponding to the high-temperature regime in the phase diagram of Fig. 2, only the bcc phase was found, while at higher segregation also the hcp was obtained. However, the hcp domain turned out to be very narrow, and the bcc phase persisted up to arbitrarily high segregation, whereas in the present case it disappears below a certain temperature. Interestingly, Fig. 2 shows that, in the temperature interval in which both phases are present, one goes from the hcp to the more loosely packed bcc clusters by *increasing* the density, and from the hcp to the bcc holes by *decreasing* the density. A qualitative explanation for this counter-intuitive behavior will be provided in a paper to come [22].

It is worth pointing out that, analogously to the two-dimensional case [8], also in three dimensions the DFT free energy functional of a SALR fluid displays a variety of local minima. Our algorithm by construction looks for periodic structures, and therefore it does not detect density profiles characterized by defects, but for a given thermodynamic state we often found periodic patterns representing local minima of the DFT functional. A few examples are shown in Fig. 10. It is tempting to interpret the occurrence of these solutions, whose free energy is only slightly higher than that
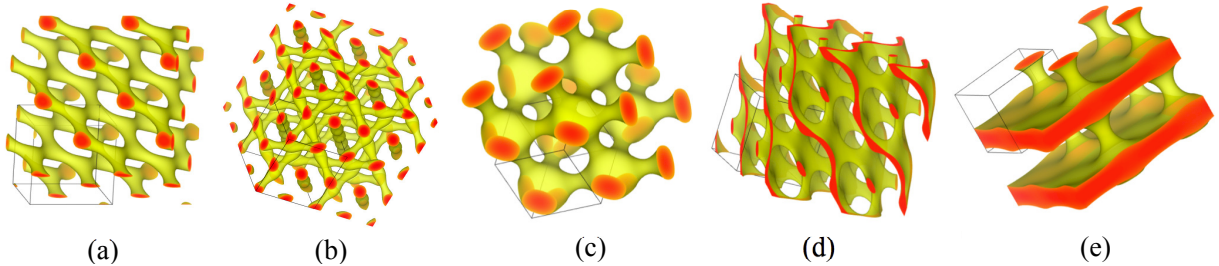
17

(a)   (b)   (c)   (d)   (e)

FIG. 10: Some periodic metastable phases found by numerical DFT minimization at $T^* = 0.6$, $\rho^* = 0.23$ (a); $T^* = 0.5$, $\rho^* = 0.24$ (b); $T^* = 0.6$, $\rho^* = 0.34$ (c) and (d); and $T^* = 0.4$, $\rho^* = 0.57$ (e).

of the stable phase, as the indication of the presence of metastable states in the physical system, although we did not attempt a thorough investigation of the free energy landscape of this model.

As a last remark, we observe that at high density a crystal phase is expected to occur because of the excluded-volume effect due to the hard-core part of the potential. However, as pointed out in Sec. II, the LDA which describes the hard-sphere interaction in functional (2) is unable to predict the occurrence of such a crystal. In order to get an estimate of the location of the fluid-solid transition, one may resort to thermodynamic perturbation theory. In this approach, the crystal is assumed to have the same fcc structure as that of the purely hard-sphere solid, and its Helmholtz free energy A_s is related to that of the hard-sphere solid A_s^HS by the expression

$$\frac{\beta A_\mathrm{s}}{V} = \frac{\beta A_\mathrm{s}^\mathrm{HS}}{V} + \frac{1}{2}\beta\rho^2 \int d^3\mathbf{r}\, g_\mathrm{s}^\mathrm{HS}(r)w(r) + \mathcal{O}(\beta^2)\,, \tag{14}$$

where $g_\mathrm{s}^\mathrm{HS}(r)$ is the radial distribution function of the hard-sphere solid averaged over the solid angle. We obtained A_s^HS by integrating with respect to ρ the equation of state of the hard-sphere solid given by Hall [31], and $g_\mathrm{s}^\mathrm{HS}(r)$ by the parametrization developed by Choi $et\ al.$ [32]. As for the fluid phase, the most straightforward choice would be using the van der Waals approximation to which Eq. (2) reduces in the homogeneous case. For the present choice of interaction parameters such that the spatial integral of the tail potential $w(r)$ vanishes, the van der Waals free energy reduces to that of the hard-sphere fluid. Another possibility is, for instance, to

18

use again perturbation theory by replacing in Eq. (14) the free energy and radial distribution function of the hard-sphere solid with the corresponding quantities of the fluid. The fluid-solid equilibrium lines are then obtained by comparing the free energies of the two phases. These lines have not been shown in Fig. 2, because we found them to be rather sensitive to the specific approximation used for the fluid, which casts some doubts on their quantitative accuracy. We just contented ourselves with the main qualitative information which they convey: first, for the tail interaction considered here, the fluid-solid transition is confined to the high-density region of the phase diagram, so that the mesophases which populate Fig. 2 are *not* prevented by freezing. This might not be the case for different interactions featuring very short-ranged attractive parts. Second, at low temperature the freezing line meets the mesophase domain at its high-density side, yielding a triple point at which the fluid, the crystal, and the inverted-hcp phases coexist. We are not in a position to provide the accurate location of the triple point, but by comparing the results given by the aforementioned approach with different recipes for the fluid free energies we may estimate its temperature and density at $T_t^* \lesssim 0.3$, $\rho_t^* \gtrsim 0.9$. A more satisfactory description of the freezing transition would require taking into account excluded-volume effects beyond the LDA in the free-energy functional.

B. The physical properties of the ordered phases

In this Section we investigate the density pattern displayed by the model in the different phases and its evolution by varying the average particle density and temperature. Here we will not consider the bicontinuous structures present in a small portion of the phase diagram because a geometrical characterization of these complex patterns would require a more detailed analysis. We limit our study to a purely phenomenological level, postponing a more quantitative investigation to a future publication [22], where the physical origin of the features highlighted by the numerical solution will be clarified.

We begin by characterizing the metric properties of the various topologies occur-

ring in the phase diagram. Figures 11-13 provide a concise summary of the parameters of the periodic structures at three representative temperatures. At relatively high temperature ($T^* = 0.7$) the modulus of the reciprocal lattice vector k_M^* identifying the highest Bragg peaks is remarkably independent of the average density, as shown in panel (a), although the topology of the ordered phase changes from a three-dimensional cluster crystal to a two-dimensional bar lattice, to a lamellar phase, moving further to the inverted structures. As also shown in Fig. 11, k_M^* is well approximated by the wave vector k_0^* of the absolute minimum in the Fourier transform of the tail potential $\widetilde{w}(k)$ (see inset in Fig. 1). In fact, as discussed in Section II, a simple mean-field argument identifies the density fluctuations responsible for the onset of the instability leading to pattern formation, precisely at such a wave vector. As a consequence of the uniformity of k_M^* at $T^* = 0.7$, the dimensionless distance d^* between neighboring maxima of the density profile is markedly constant inside each phase. The sharp discontinuity of d^* in changing the topology shown in panel (b) is a simple geometrical effect induced by the different algebraic relation between k_M^* and d^* in periodic structures of different dimensionality. Note that the inverted phases, having the same dimensionality, share the same value of d^* of the corresponding direct phase.

The independence of k_M^* from the thermodynamic state was already pointed out in the study of crystal phases of purely soft-core systems belonging to the $Q^{\pm}$ class [33] such as the generalized exponential model of order four (GEM-4) [26, 27], and stems from the same mechanism at work there, namely, the minimum of $\widetilde{w}(k)$ at $k \neq 0$. However, in that case the three-dimensional cluster phase was always found to be the most stable structure, and no transitions between phases with different dimensionality were observed. We also recall that a very satisfactory account of the properties of those soft-core systems is achieved by adopting a DFT similar to that used here, and truncating the sum over reciprocal lattice vectors in Eq. (9) at the nearest-neighbor shell [27].

When lowering the temperature, the independence of k_M^* from the average density, and the related behavior of d^*, become progressively less marked, as shown in Figs. 12
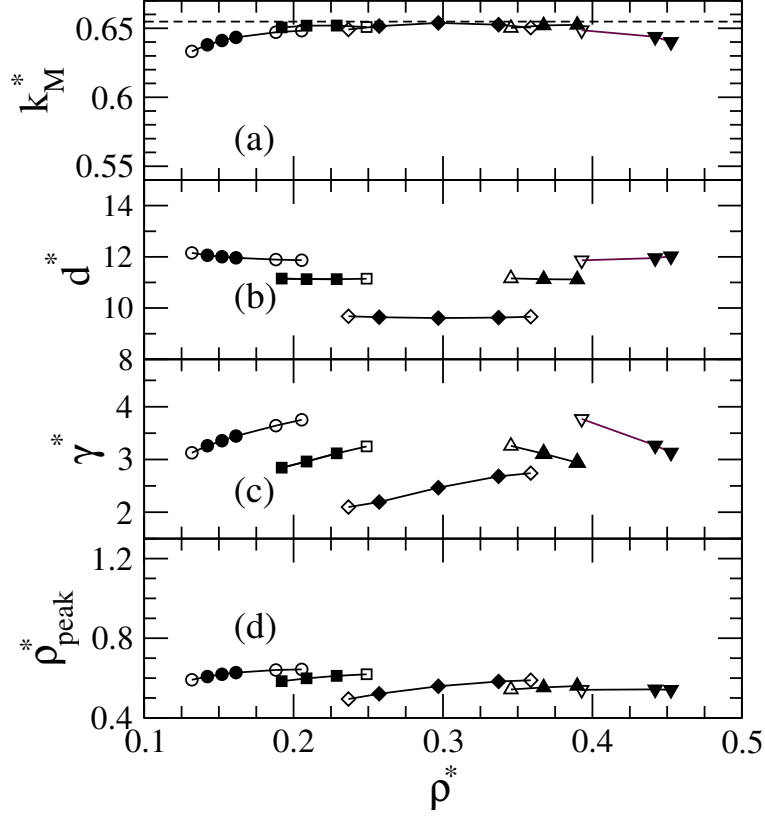
FIG. 11: Parameters of the density profile $\rho(\mathbf{r})$ at $T^* = 0.7$ as a function of the average density ρ^*. Panel (a): modulus k_{M}^* of the wave vectors of the highest Bragg peaks of $\hat{\rho}(\mathbf{k})$. Panel (b): distance d^* between neighboring peaks of $\rho(\mathbf{r})$. Panel (c): aggregate size γ^*, determined as the half-width at half maximum of the peaks. Panel (d): height ρ_{peak}^* of the peaks. All quantities are in reduced units. Different symbols represent clusters (circles), bars (squares), lamellae (diamonds), inverted bars (triangles), and inverted clusters (inverted triangles). Filled symbols denote stable phases, whereas open symbols denote phases which are either metastable or at coexistence. The dashed line in panel (a) corresponds to the wave vector of the minimum of the Fourier transform of the tail potential $\widetilde{w}(k)$.

and 13, because the instability argument loses its strength deeply inside the non-uniform region of the phase diagram, and in Eq. (9) contributions to the summation over reciprocal lattice vectors beyond nearest neighbors become more important. Nevertheless, the density dependence remains comparatively weak even at the lowest
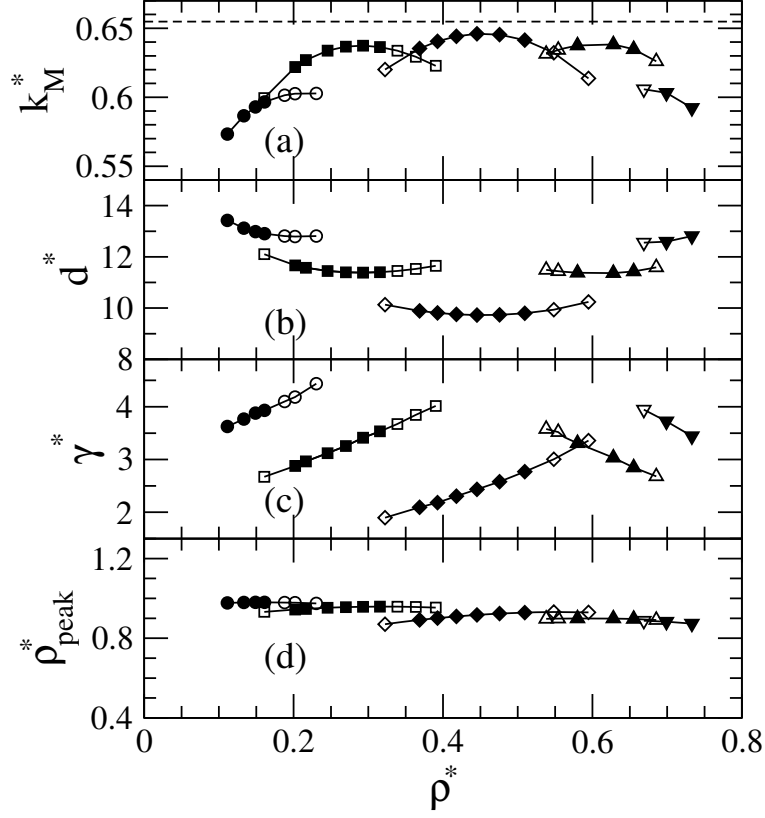
21

FIG. 12: Same as Fig. 11 at reduced temperature $T^* = 0.4$, expect that here the lattice of the cluster and inverted-cluster phases is hcp, whereas in Fig. 11 is bcc.

temperature considered here, $T^* = 0.2$.

Other important quantities for characterizing the density modulation are the width γ^* and the height ρ^*_{peak} of the density peaks. The numerical results of panels (c) and (d) respectively show that while the width of the peaks changes with ρ^*, the peak height is nearly uniform for all the three temperatures displayed in Figs. 11-13. More precisely, as ρ^* increases there is a slight decrease of ρ^*_{peak} which takes place at the transition between different phases and entails an overall decrease over the whole density axis. However, this effect is small, leading to the conclusion that, to a first approximation, ρ^*_{peak} just depends on temperature and is little affected by density. This behavior should be contrasted with that of the aforementioned soft-core $Q^{\pm}$ systems where, as the density increases, the peak height steadily increases, and the peak width steadily decreases [17].
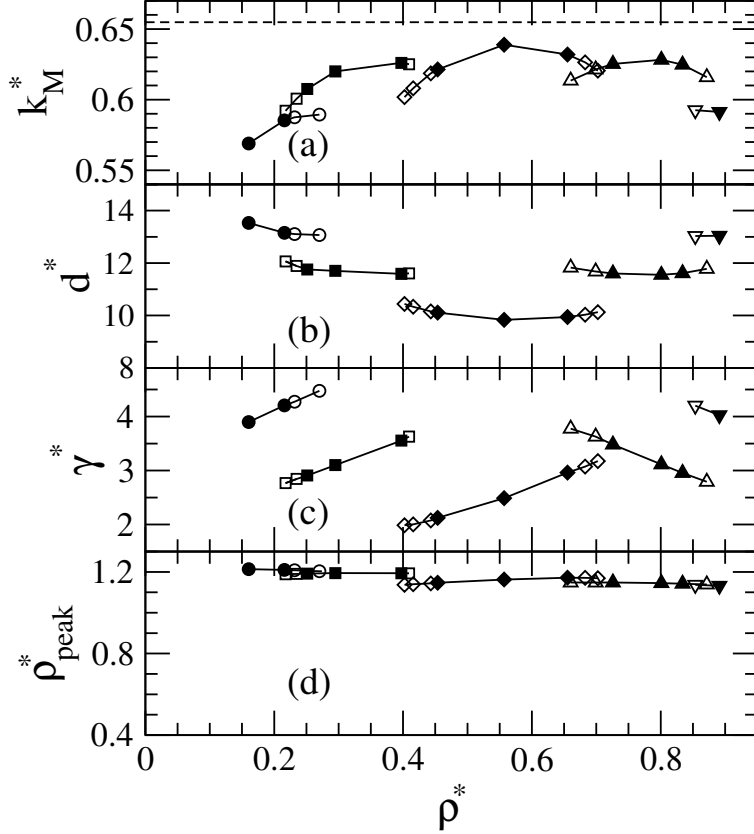
FIG. 13: Same as Fig. 12 at reduced temperature $T^* = 0.2$.

Clearly, the difference is related to the presence of excluded volume effects in our model. As noted above, for both soft-core $Q^{\pm}$ and hard-core SALR interactions the distance d^* between neighboring aggregates, irrespective of their shape, is basically determined by k_0^*, and its dependence on the density is weak or negligible. Hence, if the density increases, the system does not create more aggregates, but rather increases the population of those which already exist. In the soft-core case in which particles are allowed to overlap, the optimal free-energy gain is achieved by placing them nearly on top of each other [27], so that the mutual distance will be $\sim d^*$ for *any* two particles on neighboring lattice sites. This implies that ρ_{peak}^* increases rapidly and unboundedly with ρ.

In contrast, hard-core interactions set an upper boundary to the peak density at the close-packing value ρ_{cp}^* and, for $T \neq 0$, impose a large entropic penalty on the

free energy of configurations such that ρ^*_{peak} is near to ρ^*_{cp}. Indeed, panels (d) of Figs. 11-13 show that ρ^*_{peak} increases as T decreases and the hard-sphere entropic contribution to the free energy becomes less important, as one would expect. The function $\rho^*_{\text{peak}}(T^*)$ at constant density $\rho^* = 0.25$, corresponding to the bar phase, is shown in Fig. 14 together with a linear extrapolation to vanishing temperature. The
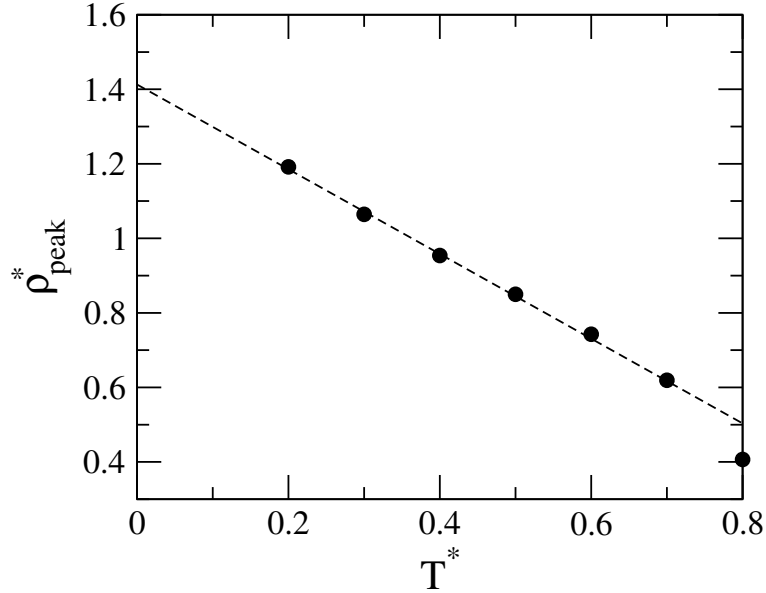

FIG. 14: Filled circles: height ρ^*_{peak} of the peaks of the reduced density profile of the bar phase at $\rho^* = 0.25$ as a function of temperature. Dashed line: linear fit over the four points at lowest temperature. Note how extrapolation at zero temperature gives the close-packing density $\rho^*_{\text{cp}} = \sqrt{2}$.

numerical data indicate that, by lowering the temperature, $\rho^*_{\text{peak}}(T^*)$ increases up to a limiting value which does coincide with the close-packing density of the hard-sphere fluid $\rho^*_{\text{cp}} = \sqrt{2}$. This result in itself is not surprising. In fact, it is found in the strong-segregation limit at $T = 0$, whereby the aggregates are described as clear-cut "objects" of constant density with a sharp interface. According to that description, the internal energy is indeed minimized when the density inside the aggregates reaches the maximum value allowed by packing restrictions [34]. What is more surprising here is that such physically sensible behavior emerges naturally from the numerical minimization, despite the fact that the Carnahan-Starling free

24

energy of the hard-sphere gas used in this study does not contain any information about the true close packing limit, placing the divergence of the compressibility at the unphysical value $\rho^* = 6/\pi > \rho^*_{\mathrm{cp}}$.

The behaviors of γ^* and ρ^*_{peak} are obviously related, since the constancy of ρ^*_{peak} at fixed temperature implies that, on increasing the average density ρ^*, the width of the peaks *within each phase* must increase in order to accommodate the larger number of particles on each lattice site. Such a relation must be reversed in the case of inverted phases, where γ^* identifies the width of the holes. A point which deserves more attention is the behavior of γ^* at the transition *between different phases*. Panels (c) of Figs. 11-13 show that at the transition from clusters to bars or from bars to lamellae, γ^* decreases significantly, whereas it increases at the transition from lamellae to inverted bars or from inverted bars to inverted clusters. Hence, as one goes through the sequence clusters-bars-lamellae-inverted bars-inverted clusters by increasing ρ^*, one witnesses a gradual growth of the domains of the direct phases, followed by an abrupt contraction when the phase with lower dimensionality takes over. Conversely, the empty domains of the inverted phases contract gradually, and expand abruptly at the transition as their dimensionality increases.

The contraction of the filled domains or the expansion of the empty domains which take place at the transition is possible without having the local density become unphysically high because, as ρ^* increases, the packing efficiency of the sequence of phases displayed by the system also increases, i.e., bars pack more efficiently than clusters, lamellae pack more efficiently than bars, and so on. However, the fact that such a process is possible does not explain in itself why this is the way actually adopted by the system to minimize its free energy.

In order to get a more complete picture and gain some insight into this point, in Figs. 15-17 we have considered the difference $\beta \Delta F/N$ between the Helmholtz free energy per particle and unit temperature of the inhomogeneous phases and that of the homogeneous phase as well as its energetic contribution $\beta \Delta E/N$ and entropic contribution $-\Delta S/(k_{\mathrm{B}} N)$. These quantities have been plotted as a function of ρ^* in

panels (a), (b), and (c) respectively for the same isotherms considered in Figs. 11-13. In order to enable the comparison between different phases, each of them has been significantly extended into its metastable region.
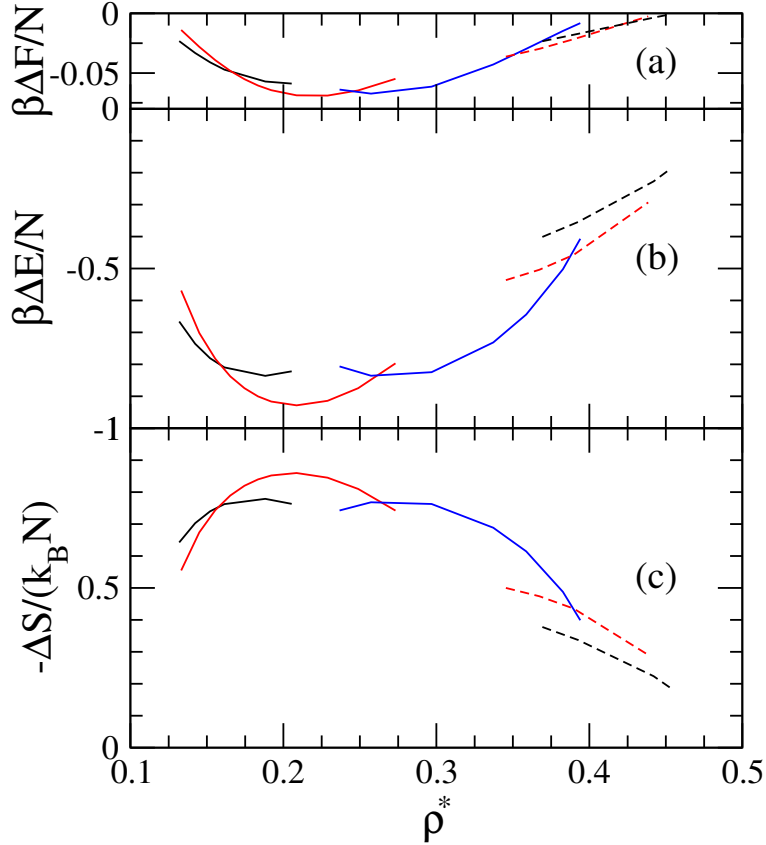

FIG. 15: Panel (a): difference $\beta\Delta F/N$ between the Helmholtz free energy F per particle and unit temperature of the ordered phases and that of the homogeneous fluid as a function of the reduced density ρ^* at $T^* = 0.7$. Black solid line: clusters. Red solid line: bars. Blue solid line: lamellae. Red dashed line: inverted bars. Black dashed line: inverted clusters. Each phase has been substantially extended into its metastable region. Panel (b): same as panel (a) for the difference $\beta\Delta E/N$ in the internal energies per particle and unit temperature. Panel (c): same as panel (a) for the difference $-\Delta S/(k_B N)$ in minus the entropies per particle.

First we observe that, as one would expect, ΔS and ΔE are both negative at all temperatures and densities, i.e., the formation of ordered structures entails en
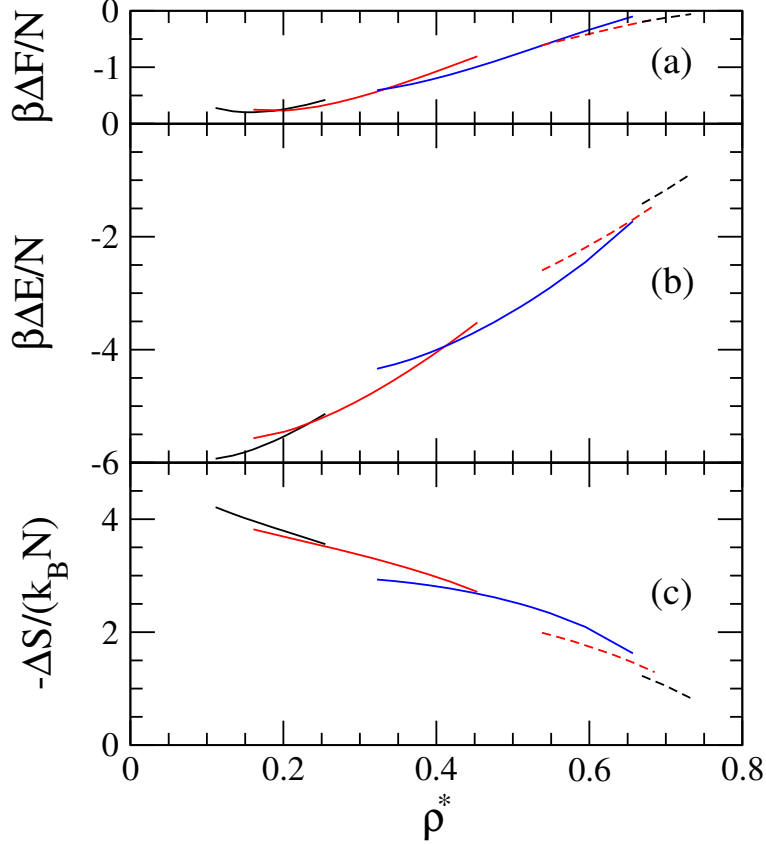
26

FIG. 16: Same as Fig. 15 at $T^* = 0.4$.

entropic penalty with respect to the homogeneous phase, which has then to be counteracted by a decrease (increase in absolute value) of the internal energy. Indeed, the entropic and energetic contributions are nearly specular so that, for each phase, an increase of the entropic penalty is accompanied by an increase of the energetic gain.

Moreover, if we rule out the low-density interval $\rho^* \lesssim 0.2$ at $T^* = 0.7$, there is a general trend for the entropic penalty to decrease as ρ^* increases, meaning that the average volume available to each particle becomes closer to that of the homogeneous phase. At the same time, the energetic advantage with respect to the homogeneous phase also decreases because, as more and more particles are added to the system, it becomes more and more difficult to obtain an arrangement such that a large amount of them will be at a distance $\sim d^*$ from each other. Basically, one has to content oneself with whatever space is left.
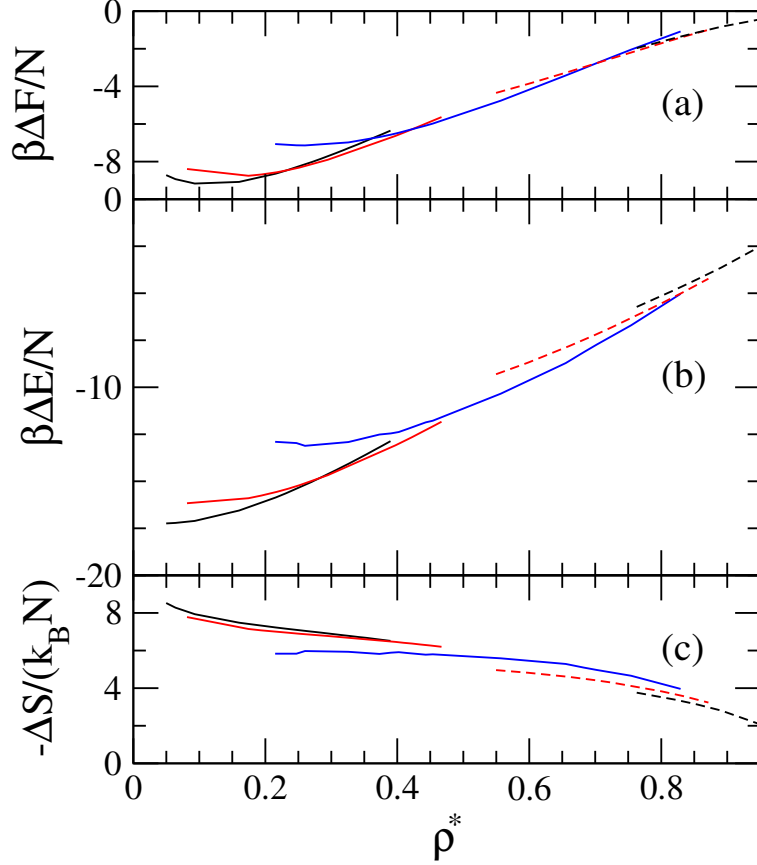
FIG. 17: Same as Fig. 15 at $T^* = 0.2$.

The above observations hold irrespective of the specific phase one is considering. If we now focus on the transitions between different phases and locate them at the points where the free energies of the phases involved cross, we do find that in most cases the phase which takes over as ρ^* increases has the larger entropy. However, this is not always true, see the aforementioned low-density interval at $T^* = 0.7$. Even when it is, the entropies are quite similar and, contrary to what one would expect, their difference generally decreases as ρ^* is further increased. On the face of this, one might envisage an alternate scenario with respect to that displayed in panels (c) of Figs. 11-13, whereby the characteristic domain size γ^* would be left nearly unchanged when going from a phase to another. In that case, the phase which packs better would be given a much larger entropic advantage over the other because of the larger volume available to particles at given ρ^*. Why doesn't the system follow this strategy, instead

of squeezing γ^* to the point that most of this advantage gets lost?

The answer lies in the fact that such a large entropic advantage would entail a large increase (decrease in absolute value) of the internal energy. In contrast, the comparison between panels (a) and (b) of Figs. 15-17 shows that as ρ^* increases, the internal energy plays a key role in stabilizing the configurations of lower dimensionality or, conversely, those of higher dimensionality for the inverted phases. In fact, the branches of ΔF and ΔE corresponding to different phases cross in essentially the same sequence, even though not at the same densities. Moreover, such a sequence persists down to $T \to 0$, when the entropic contribution becomes negligible. This role of the internal energy is achieved precisely by changing γ^* so as to narrow the domains occupied by the particles. The mechanism at play is not specific to the SALR potential considered here, but applies to all interactions consisting of a hard-core part and a tail whose Fourier transform has its absolute minimum at $k \neq 0$, such as, for instance, a repulsive square shoulder [21], and will be described in detail elsewhere [22].

Finally, in Figs. 18-20 we show the density profile along the direction connecting the nearest neighbors of the ordered structures for the bcc cluster phase, the bar phase, and the lamellar phase. For each phase, the upper and lower panels refer to $T^* = 0.7$ and $T^* = 0.4$ respectively.

At the lower temperature, the density profile presents a sharp interface which separates filled and empty regions, indicating the occurrence of well-defined geometrical structures in the system. Moreover, as also shown in Fig. 12(d), ρ^*_{peak} attains rather high values, comparable to the freezing density of the bulk hard-sphere fluid. In this regime, the density profile is expected to show also significant modulations on a lengthscale $\sim \sigma$ because of packing effects, such as those displayed in Fig. 5 of Ref. [20], but the LDA is unable to account for them as it is not powerful enough to resolve the inner structure of the aggregates.

Instead, at the higher temperature the ordered phase is more appropriately interpreted in terms of a periodic density modulation on top of a uniform fluid. The
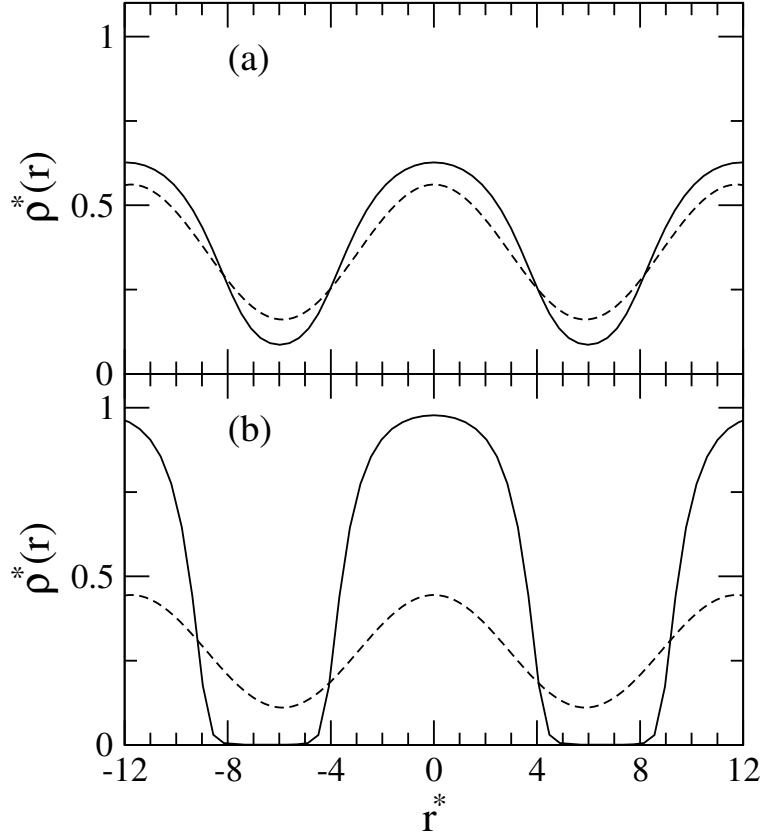
FIG. 18: Reduced density profile $\rho^*(\mathbf{r})$ along the line connecting nearest-neighbor sites for the cluster bcc phase at $T^* = 0.7$, $\rho^* = 0.16$ (panel (a)) and $T^* = 0.4$, $\rho^* = 0.11$ (panel (b)). In both panels, the solid line is the result of the unconstrained minimization of functional (2), whereas the dashed line has been obtained by expanding $\rho^*(\mathbf{r})$ around the uniform state $\rho^*(\mathbf{r}) \equiv \rho^*$ (see text). According to the unconstrained minimization, the bcc phase at $T^* = 0.4$ (panel b) is metastable with respect to the hcp phase.

competitive nature of the SALR potential stabilizes such a corrugation, suggesting that the minimization procedure may be considerably simplified in this regime, by parametrizing the density profiles as the sum of its average value plus a sinusoidal modulation characterized by wave vectors whose moduli are fixed equal to the value k_0, so as to minimize the Fourier transform of the spherically symmetric tail potential. The different possible topologies (BCC crystals, bar crystals and lamellar phases) then give rise to density profiles uniquely parametrized by the amplitude of the modulation. The equilibrium density profiles resulting from the minimization of
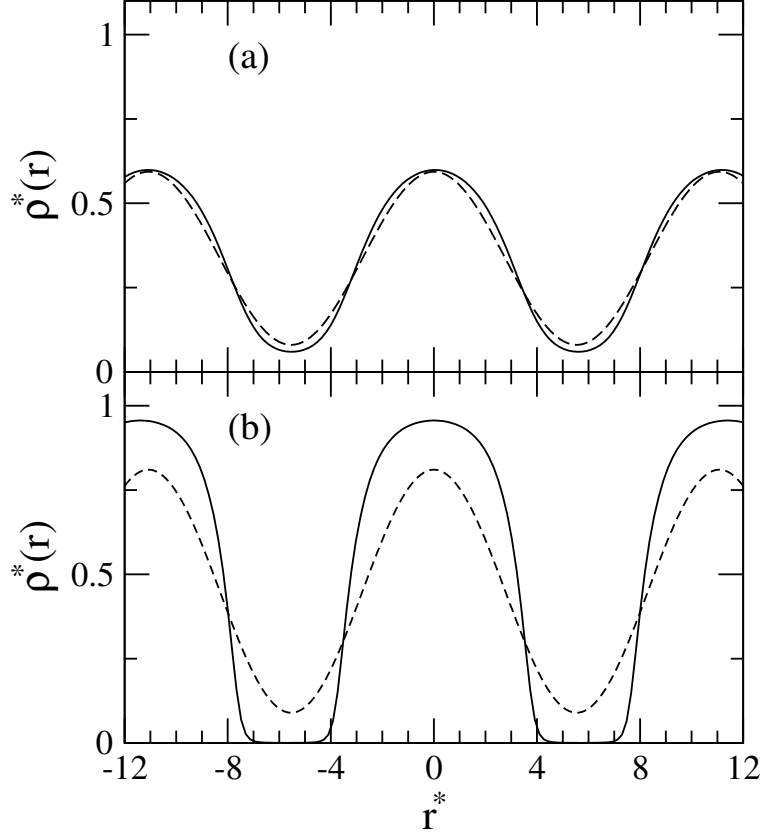
FIG. 19: Same as Fig. 18 for the bar phase at $T^* = 0.7$, $\rho^* = 0.21$ (panel (a)) and $T^* = 0.4$, $\rho^* = 0.27$ (panel (b)).

DFT functional (2) within this analytic parametrization have also been displayed in the Figures.

The comparison between the two sets of results shows that, although the validity of such an approach for a qualitative understanding of the phase diagram is not in question, its quantitative accuracy is limited to relatively high temperatures: at $T^* = 0.7$, the analytic $\rho^*(\mathbf{r})$ compares rather satisfactorily with the output of the numerical minimization, with somehow larger errors the higher the dimensionality of the equilibrium structures, whereas at $T^* = 0.4$ the agreement is qualitative at most. The largest discrepancies are again obtained for the bcc phase, see panel (b) of Fig. 18. Please note that, according to the present study, the most stable phase for the state to which Fig. 18(b) refers is actually the hcp, but we have chosen to
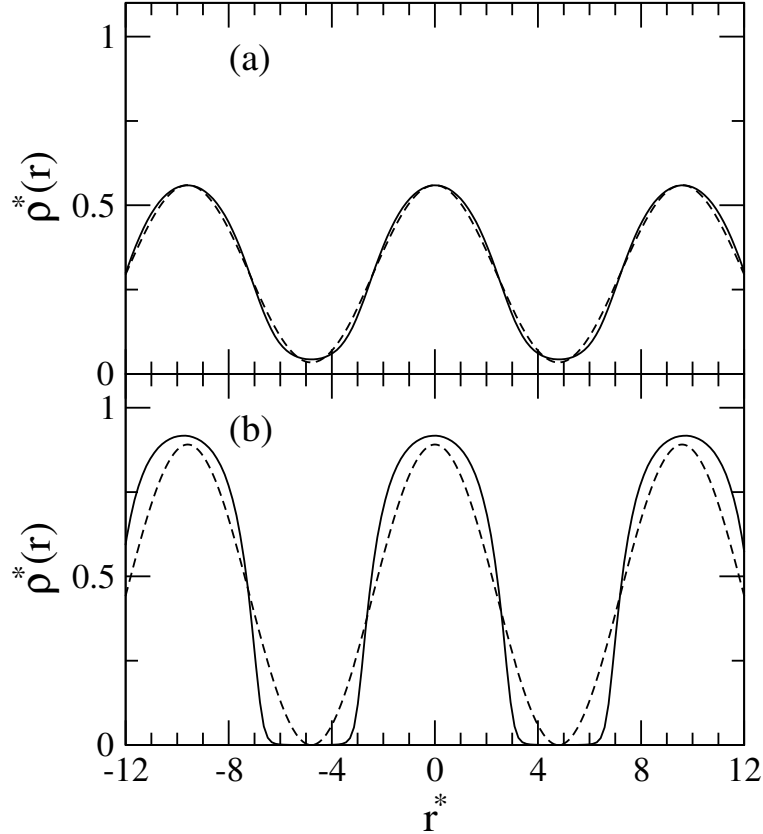
FIG. 20: Same as Fig. 18 for the lamellar phase at $T^* = 0.7$, $\rho^* = 0.30$ (panel (a)) and $T^* = 0.4$, $\rho^* = 0.45$ (panel (b)).

display the bcc because this is the structure predicted by parametrizing the density profile as a sinusoidal modulation, in order to compare the two approaches on as much an equal footing as possible. Anyway, the qualitative picture would have remained unchanged by considering the hcp phase. The relevant point is that, despite the low value of the average density ρ^*, the numerical solution still presents a sharp variation of $\rho^*(\mathbf{r})$. Such a situation cannot be described by the analytic $\rho^*(\mathbf{r})$, because the superposition of a large-amplitude modulation to a low uniform background would force it to become unphysically negative in some region. In fact, in this regime the amplitude saturates at its largest value compatible with the requirement that $\rho(\mathbf{r})$ be everywhere non-negative.

IV. CONCLUSIONS

In this work we investigated a model often adopted to represent suspensions of charged nanoparticles, consisting of a hard-core potential followed by a short-range attractive and long-range repulsive (SALR) tail. The equilibrium configurations of the system have been determined by a fully numerical minimization of a simple, mean-field free energy functional, and the phase diagram thus obtained compares well with the available results from a recent study based on similar techniques [20]. Below a limiting temperature, signaling the instability of the homogeneous phase, the model is shown to display a sequence of first-order phase transitions between periodic structures: starting from a three-dimensional cluster crystal at low density, a bar phase develops, whereby the density profile displays cylinders arranged in a triangular lattice, which is followed by a lamellar arrangement. Then, if the density is further increased, inverted phases appear, reproducing in reverse order the same sequence of transitions. Close to the boundaries of the lamellar phase, two bicontinuous density modulations appear at low temperature. The very same sequence of ordered phases has been predicted by analytical studies of a long-wavelength approximation of the free-energy functional [2, 12] and appears to be a robust feature of a large class of systems, ranging from hard-core fluids with competing interactions like that investigated here [11, 12, 20, 21] to hard-core fluids with a soft repulsive shoulder [21], to block copolymers [2]. The relevant wave-vector, defining the periodicity of the structures, is seen to be largely determined by the location of the minimum of the Fourier transform of the tail potential. Therefore, at least at moderate temperature, the density modulations are characterized by a lengthscale independent of the thermodynamic state of the system, which determines the distance between neighboring density peaks in each topology. The characteristic peak density is seen to depend mainly on temperature, implying that, by increasing the average density of the system, the width of the density peaks of the direct phases increases up to the transition point, where it sharply decreases as soon as the phase with lower dimensionality takes over. Conversely, the size of the particle-depleted regions of the

inverted phases decreases within each phase, and increases at the transition.

Although the numerical calculations show that the free energy differences between all the stable phases are very small, the predicted sequence of transitions appears to be largely independent of the details of the adopted model. Even the very narrow stability regions of the gyroid phase is a common feature of several systems, implying that a fine tuning of parameters is required to select such a phase in the available theoretical models. It is worth observing that a previous investigation of a soft-core binary mixture based on the same method [18] has uncovered a very rich phase diagram which displays several common features with that considered here, but also some important differences, such as a much stronger propensity to form bicontinuous phases. It would be interesting to pinpoint the reason for this different behavior.

The numerical free-energy minimization method used here holds a potential for a number of applications. Besides the periodic phases formed in bulk three-dimensional systems, a similar method could be employed also for the study of the structures obtained by the SALR or related potentials on a curved substrate. We plan to consider such a case in the near future.

---

[1] See, for instance, J. N. Israelachvili, "Intermolecular and Surface Forces" (Academic Press, London), 1998.

[2] L. Leibler, Macromolecules **13**, 1602 (1980); M. W. Matsen, J. Phys.: Condens. Matter **14**, R21 (2002).

[3] B. M. Mladek, G. Kahl, and C. N. Likos Phys. Rev. Lett. **100**, 028301 (2008).

[4] D. A. Lenz, B .M. Mladek, C. N. Likos, G. Kahl, and R. Blaak J. Phys. Chem. B **115**, 7218 (2011).

[5] M. A. Glaser, G. M. Grason, R. D. Kamien, A. Kosmrlj, C. D. Santangelo, and P. Zhierl, EPL **78**, 46004 (2007); G. Pauschenwein and G. Kahl, Soft Matter **4**, 1396 (2008); J. Chem. Phys. **129**, 174107 (2008).

[6] R. P. Sear, S.-W. Chung, G. Markovich, W. M. Gelbart, and J. R. Heath Phys. Rev.

E **59** R6255 (1999); R. P. Sear and W. M. Gelbart, J. Chem. Phys. **110**, 4582 (1999).

[7] A. Imperio and L. Reatto, J. Phys.: Condens. Matter **16** S2769 (2004); J. Chem. Phys. **124**, 164712 (2006).

[8] A. J. Archer, Phys. Rev. E **78**, 031402 (2008).

[9] A. Stradner, H. Sedwick, F. Cardinaux, W. C. K. Poon, S. U. Egelhaaf, and P. Schurtenberger, Nature (London) **432**, 492 (2004); A. I. Campbell, V. J. Anderson, P. Bartlett, and J. S. van Duijenveldt, Phys. Rev. Lett. **94**, 208301 (2005).

[10] A. J. Archer and N. B. Wilding, Phys. Rev. E **76**, 031501 (2007).

[11] Y. Zhuang, K. Zhang, and P. Charbonneau, Phys. Rev. Lett. **116**, 098301 (2016).

[12] A. Ciach, Phys. Rev. E **78**, 061505 (2008); A. Ciach and W. T. Góźdź, Condens. Matter. Phys. **13**, 2603 (2010).

[13] M. B. Sweatman, R. Fartaria, and L. Lue, J. Chem. Phys. **140**, 124508 (2014).

[14] See for instance J.-P. Hansen and I. R. McDonald "Theory of Simple Liquids" (Academic Press, London), 2013.

[15] M. Carta, D. Pini, A. Parola, and L. Reatto, J. Phys.: Condens. Matter **24**, 284106 (2012).

[16] M. Parrinello and A. Rahman, Phys. Rev. Lett. **45**, 1196 (1980).

[17] D. Pini, Trans. R. Norw. Soc. Sci. Lett. **3**, 99 (2014).

[18] D. Pini, A. Parola, and L. Reatto J. Chem. Phys. **143**, 034902 (2015).

[19] A. J. Archer, C. N. Likos, and R. Evans J. Phys.: Condens. Matter **16**, L297 (2004).

[20] M. Edelmann and R. Roth, Phys. Rev. E **93**, 062146 (2016).

[21] H. Shin, G. M. Grason, and C. D. Santangelo, Soft Matter **5**, 3629 (2009).

[22] D. Pini, to be submitted.

[23] A. J. Archer, D. Pini, R. Evans, and L. Reatto, J. Chem. Phys. **126**, 014104 (2007).

[24] A. J. Archer, C. Ionescu, D.Pini, and L. Reatto, J. Phys.: Condens. Matter **20**, 415106 (2008).

[25] Y. Rosenfeld, Phys. Rev. Lett. **63**, 980 (1989); R. Roth, J. Phys.: Condens. Matter **22**, 063102 (2010).

[26] B. M. Mladek, D. Gottwald, G. Kahl, M. Neumann, and C. N. Likos, Phys. Rev. Lett.

96, 045701 (2006); **97**, 019901 (2006)

[27] C. N. Likos, B. M. Mladek, D. Gottwald, and G. Kahl, J. Chem. Phys. **126**, 224502 (2007).

[28] K. von Konigslow, E. D. Cardenas-Mendez, R. B. Thompson, and K. Ø. Rasmussen, J. Phys.: Condensed Matter **25**, 325101 (2013).

[29] K. Momma and F. Izumi, J. Appl. Crystallogr. **44**, 1272 (2011).

[30] M. W. Matsen and F. S. Bates, Macromolecules **29**, 1091 (1996); M. W. Matsen, J. Phys.: Condens. Matter **14**, R21 (2002); M. W. Matsen, Eur. Phys. J. E **30**, 361 (2009).

[31] K. R. Hall, J. Chem. Phys. **57**, 2252 (1972).

[32] Y. Choi, T. Ree, and F. H. Ree, J. Chem. Phys. **95**, 7548 (1991).

[33] C. N. Likos, A. Lang, M. Watzlawek, and H. Löwen, Phys. Rev. E **63**, 031206 (2001).

[34] A. Košmrlj, G. J. Pauschenwein, G. Kahl, and P. Ziherl, J. Phys. Chem. B **115**, 7206 (2011).